

# Resolving space-time structures of quantum impurities with a numerically-exact algorithm using few-body revealing

Yuriel Núñez Fernández,<sup>1</sup> Maxime Debortolis,<sup>2</sup> and Serge Florens<sup>1</sup>

<sup>1</sup>*Univ. Grenoble Alpes, CNRS, Grenoble INP, Institut Néel, 38000 Grenoble, France*

<sup>2</sup>*Institute of Physics, University of Bonn, Nussallee 12, 53115 Bonn, Germany*

We introduce a numerically exact real-time evolution scheme for quantum impurities in a macroscopically large bath. The algorithm is *few-body revealing*, namely it identifies the electronic orbitals that can be made inactive (in a trivial product state) by a time-dependent orbital rotation. Following a quench, we show that both the number of active orbitals and their associated matrix product state bond dimensions saturate to small values, leading to an algorithm dramatically more accurate and faster than the state of the art. We are thus able to follow the dynamics for thousands of fermions, up to the long-time stationary regime, and to study subtle aspects of quantum relaxation in the spatio-temporal domain, such as the emergence of entanglement structures in the Kondo screening cloud.

The many-body dynamics of generic quantum systems currently challenges numerical simulations, as exemplified by the unbounded entanglement growth in time of matrix product states (MPS). This situation also plagues quantum impurity problems, “simpler” systems still comprised of a macroscopic number of particles (bosons or fermions), where the interaction is restricted to a subset of degrees of freedom [1]. The interest in impurity models, originating in Kondo physics, has not waned over the years, since they are the cornerstone of the Dynamical Mean-Field Theory (DMFT) for correlated electrons [2]. Open quantum systems, in which qubits exchange energy and information with an environment, constitute also a very important class of impurity models [3]. However, in most cases, simulating the real-time non-perturbative dynamics of impurity models comes with tremendous numerical cost: typical runs taking over a week only achieve a limited 1% accuracy on observables for quenches, and relatively short reachable time scales [4, 5]. Progress is often made by losing the information over the spatial dynamics of the environment [6–13].

We pose in this Letter the idea of *few-body revealing* for quantum impurities models, based on a new finding that their quench dynamics involves only a small number of entangled environmental degrees of freedom, called *active orbitals*, that continuously adapt during the time evolution. The rest of the macroscopic environment remains at each time in a trivial, yet evolving, product state (Slater determinant for fermions), making the simulation of systems with thousands of sites now reachable. Entanglement growth is prevented by collecting at each time step the orbital rotation into an *evolving unitary frame* that is never applied to the state (this would make the problem many-body again), but only to observables. Our main advance is to propose a *numerically exact algorithm* (with controllable errors below  $10^{-6}$ ) that takes advantage of this few-body structure, leading to a drastic reduction of the computing time (down to only minutes for full relaxation of systems with hundreds of sites),

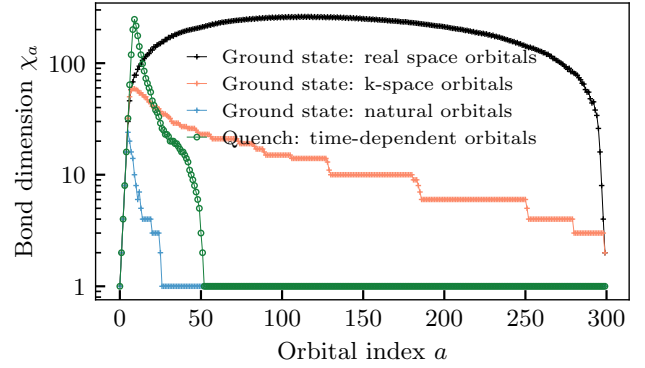


Figure 1. Demonstrating *few-body revealing* from the MPS bond dimension  $\chi_a$  as a function of orbital index  $a$ , for the IRLM with  $L = 300$  sites at  $U/D = -0.5$  and  $V/D = 0.1$ . For ground states (crosses), natural orbitals show a drastic compression w.r.t. real-space and k-space orbitals, because all natural orbitals with  $\chi_a = 1$  are contained in a Slater state. For the dynamics following a quench (circles), an optimal orbital rotation leaves the state vector  $|\psi(t)\rangle$  few-body at the long time  $D.t = 100$ , while  $\chi_a$  would exceed here  $10^4$  for real-space and k-space, making the computation unfeasible.

while giving access to real space information on the environment. This algorithm allows us to study the buildup of the dynamical Kondo cloud after a quench, uncovering new aspects of decoherence in a fermionic environment.

*Model.* We consider the Interacting Resonant Level model (IRLM) [14] given by the real space Hamiltonian in terms of local fermion operators  $\hat{c}_i^\dagger$  and charges  $\hat{n}_i = \hat{c}_i^\dagger \hat{c}_i$ :

$$\hat{H} = U \left( \hat{n}_0 - \frac{1}{2} \right) \left( \hat{n}_1 - \frac{1}{2} \right) + \epsilon_0(t) (\hat{n}_0 - \hat{n}_1) + V (\hat{c}_0^\dagger \hat{c}_1 + \hat{c}_1^\dagger \hat{c}_0) + \frac{D}{2} \sum_{i=1}^{L-2} (\hat{c}_{i+1}^\dagger \hat{c}_i + \text{h.c.}), \quad (1)$$

with interaction  $U$ , hybridization  $V$ , and hoppings  $D/2$ . The time-dependent impurity onsite energy will be quenched from  $\epsilon_0(t) = -\infty$  at  $t < 0$  (so that sites 0

and 1 are initially decoupled from the bath), to  $\epsilon_0(t) = 0$  at  $t > 0$ . The IRLM is a very good testbed for quantum impurities since it exhibits Kondo correlations at  $U < 0$  in the charge sector.

A first insight onto the problem is given by the matrix product state (MPS) bond dimension distribution  $\chi_a$  for the ground state of the IRLM (at fixed  $\epsilon_0 = 0$ ), see Fig. 1. We observe a huge compression when using the natural orbital basis, namely when solving Hamiltonian (1) in the set of fermionic operators  $\sum_i U_{ai} \hat{c}_i$  that diagonalize the correlation matrix  $\rho_{ij} = \langle \hat{c}_i^\dagger \hat{c}_j \rangle$ . Not only the bond dimension is much smaller for natural orbitals than for real-space and k-space orbitals, but also the number of active orbitals is less than 40 (this is nearly independent of the system size), meaning that almost all the orbitals are in a perfect product state (Slater determinant). This is in agreement with previous studies based on iterative diagonalization [15–17] and non-Gaussian states [18–22]. One important finding of this Letter is that a time-dependent orbital rotation maintains this few-body picture at any time after a local quench, as can be seen from the curve of Fig. 1 in circle symbols. We now present the algorithm allowing us to obtain controlled calculations for the quench at long times, taking advantage of the few-body picture.

*General frame evolution.* We propose that the physical state at a given time  $t$  is given by  $\exp[-i\hat{F}(t)]|\psi(t)\rangle$ , where  $\hat{F}(t) = \sum_{a,b=0}^{L-1} F_{ab}(t) \hat{c}_a^\dagger \hat{c}_b$  is a quadratic form in terms of fermion operators, parametrized by an hermitian one-body matrix  $F_{ab}(t)$  that we call *frame*. Previous studies have shown disentangling properties of orbital rotations, but were limited by a fixed time-independent frame [23]. Other similar approaches did not take advantage of the further simplifications brought by impurity models [24, 25]. Picking an optimal frame  $F_{ab}(t)$  will keep a very low entanglement in the many-body wavefunction  $|\psi(t)\rangle$  for the whole time evolution. This is possible because for the quench dynamics of impurity models, only a small number of active orbitals  $N_{\text{active}} \ll L$  is involved in  $|\psi(t)\rangle$ , as hinted in Fig. 1. From Thouless theorem [26], the change of frame transforms each orbital to a linear combination as

$$\exp[i\hat{F}(t)]\hat{c}_a \exp[-i\hat{F}(t)] = \sum_b [e^{-iF(t)}]_{ab} \hat{c}_b. \quad (2)$$

Importantly, we restrict the rotation  $F_{ab}$  only to the bath orbitals (namely to sites  $i > 1$  in our model), in order to leave the interaction term of the impurity unaffected.

*Trotterized evolution.* We notice that the application of a general orbital rotation  $\exp[-i\hat{F}(t)]$  to a given MPS  $|\psi(t)\rangle$  is as expensive as a full time evolution, and should be avoided at all costs. The first trick is to separate the time evolution between two parts: a macroscopic part stemming only from the *bath* variables (namely sites  $i = 2, \dots, L-1$ ), that is never applied to the state  $|\psi(t)\rangle$ , and a microscopic part that is efficiently

applied to  $|\psi(t)\rangle$  using shallow quantum gates. Evolution is performed by splitting the bath Hamiltonian  $\hat{H}_{\text{bath}} \equiv (D/2) \sum_{i=2}^{L-2} (\hat{c}_i^\dagger \hat{c}_{i+1} + \text{h.c.})$  from the impurity part  $\hat{H}_{\text{imp}} \equiv \hat{H} - \hat{H}_{\text{bath}}$ . While the operator  $\hat{H}_{\text{bath}}$  accounts for most of the energy of the system for large  $L$ , it is a quadratic Hamiltonian whose associated time evolution corresponds to an orbital rotation that can be incorporated into the frame  $F_{ab}(t)$ . To isolate the macroscopic bath operator from the impurity one, we perform a Trotter time evolution on a small interval  $dt$  using the third order Baker–Campbell–Hausdorff formula:

$$e^{-i\hat{H}dt} = e^{-i\hat{H}_{\text{bath}}dt} e^{-i\hat{H}_{\text{imp}}dt} \approx e^{-i\hat{H}_{\text{bath}}dt} e^{-i\hat{H}_{\text{imp}}^{(2)}dt}. \quad (3)$$

The first term is incorporated to a new frame  $F(t+dt)$ , and only the second term drives the time evolution with a dressed Hamiltonian  $\hat{H}_{\text{imp}}^{(2)} = \hat{H}_{\text{imp}} - idt[\hat{H}_{\text{imp}}, \hat{H}_{\text{bath}}]/2$ .  $\hat{H}_{\text{imp}}^{(2)}$  is expressed in the current frame  $F(t)$ , which rotates only bath orbitals. The interaction term  $U\hat{n}_0\hat{n}_1$  and hybridization  $V(\hat{c}_0^\dagger\hat{c}_1 + \hat{c}_1^\dagger\hat{c}_0)$  are both invariant under bath rotations, and only the coupling term  $(D/2)\hat{c}_1^\dagger\hat{c}_2$  (and its order  $dt$  correction) is affected. After frame rotation according to Eq. (2),  $\hat{H}_{\text{imp}}^{(2)}$  takes the form:

$$\hat{H}_{\text{imp}}^{(2)} = U\hat{n}_0\hat{n}_1 + V(\hat{c}_0^\dagger\hat{c}_1 + \hat{c}_1^\dagger\hat{c}_0) + \sum_{a,b=0}^{L-1} K_{ab} \hat{c}_a^\dagger \hat{c}_b. \quad (4)$$

For the IRLM, the matrix  $K_{ab}$  couples only site  $i = 1$  to a linear combination of bath fermions, and is therefore rank 1 (in general its rank is the number of electronic channels coupling to the impurity).

*Few-body evolution.* We re-express Hamiltonian (4) in terms of the orbital  $\hat{f}_2$  coupling to  $c_1^\dagger$  through  $K_{ab}$ :

$$\hat{H}_{\text{imp}}^{(2)} = U\hat{n}_0\hat{n}_1 + V(\hat{c}_0^\dagger\hat{c}_1 + \hat{c}_1^\dagger\hat{c}_0) + K(\hat{c}_1^\dagger\hat{f}_2 + \hat{f}_2^\dagger\hat{c}_1). \quad (5)$$

Therefore, the time evolution will be trivial (few-body) if we can efficiently rotate the MPS state  $|\psi(t)\rangle$  into this appropriate basis. This can be achieved by an intra-bath rotation  $Q_{\text{few}}$  that is associated to the first right singular vector of  $K_{ab}$  (see Ref. [27] and Sec. I of Ref. [28]).

In practice, we also need to perform this rotation so that its action on the bath keeps the state few-body. The trick is to classify at a given time bath orbitals into three groups according to their occupation number  $n_a = \langle \hat{c}_a^\dagger \hat{c}_a \rangle$ : *empty* ( $0 \leq n_a \leq \epsilon$ ), *full* ( $1 - \epsilon \leq n_a \leq 1$ ), and *active* ( $\epsilon < n_a < 1 - \epsilon$ ), with  $\epsilon$  a small cutoff (typically  $10^{-10}$  or less). At order  $\epsilon$ , we can thus consider that empty/full orbitals are strictly inactive, namely  $n_a = 0$  or  $n_a = 1$ , so that any rotation of the empty or full orbitals (that does not mix them) now leaves the corresponding Slater determinant invariant. By doing the rotation  $Q_{\text{empty}}$  (resp.  $Q_{\text{full}}$ ) that extracts the first right singular vector of matrix  $K_{ab}$  in the empty (resp. full) sector, we obtain that all empty (full) orbitals are isolated except the first one. If the state at a given time

$t$  had  $N_{\text{active}}$  active orbitals, the evolved state at time  $t + dt$  will have  $N_{\text{active}} + 2$  active ones, and all inactive orthogonal bath orbitals will still remain in a (rotated) Slater state.

*Orbitals optimization.* After evolving the state  $|\psi(t)\rangle$ , its optimal frame has changed and must be adapted to reduce the entanglement within the new set of  $N_{\text{active}} + 2$  active orbitals. A set of local rotations  $Q_{\text{opt}}$  can diagonalize the correlation matrix  $\rho_{ab} = \langle \psi | \hat{c}_a^\dagger \hat{c}_b | \psi \rangle$  among the  $N_{\text{active}} + 2$  active orbitals only, since the remaining  $L - (N_{\text{active}} + 2)$  orbitals are either empty or full. The diagonalization is done as proposed in [27] for Slater states. We use nearest neighbor Givens rotations [29] to extract the extremum eigenpair of the correlation matrix (see Sec. I of Ref. [28]), and repeating this process up to visiting all eigenpairs. After this step, the number of active orbitals most often goes back to the previous value  $N_{\text{active}}$  only, and its total increase over the whole temporal simulation will assess how few-body the state has stayed. These local rotations are finally mapped to local quantum gates that are efficiently applied to the state  $|\psi(t)\rangle$ , bringing it in the new frame.

*The few-body revealing algorithm.* To summarize, our algorithm operates by simple iterative updates of the frame matrix  $F_{ab}(t)$ , and by a few-body evolution of the state  $|\psi(t)\rangle$  for each time step  $dt$ , as follows:

- (I) *Trotterized evolution:* The frame is updated as  $\exp(-iF) \leftarrow \exp(-iH_{\text{hop}}dt)\exp(-iF)$  from the Trotter decoupling, where  $[H_{\text{hop}}]_{ij} = (D/2)\delta_{i,j\pm 1}$  is the hopping matrix appearing in  $\hat{H}_{\text{bath}}$ .
- (II) *Few-body evolution:* The frame is updated as  $\exp(-iF) \leftarrow \exp(-iF)Q_{\text{empty}}Q_{\text{full}}Q_{\text{few}}$ , and we map  $Q_{\text{few}}$  to a shallow quantum circuit that we apply to the state  $|\psi(t)\rangle$ . The state is then time-evolved by block decimation [30, 31] upon  $\hat{H}_{\text{imp}}^{(2)}$  that acts only on three orbitals, and  $N_{\text{active}} + 2$  orbitals are now active.
- (III) *Orbital optimization:* The frame is updated as  $\exp(-iF) \leftarrow \exp(-iF)Q_{\text{opt}}$ , and  $Q_{\text{opt}}$  is mapped as a shallow quantum circuit to the state  $|\psi(t)\rangle$ . The number of active orbitals most often drops back to  $N_{\text{active}}$ , and the entanglement is reduced.

The error in step (I) is  $\mathcal{O}(dt^3)$ , due to Eq. (3). Step (II) introduces an error  $\mathcal{O}(\epsilon)$  from the threshold  $\epsilon$  used to freeze the nearly empty and full orbitals. We additionally compress the MPS with the same tolerance  $\epsilon$  after applying the gates in steps (II-III). The error in the few-body time evolution of the MPS is  $\mathcal{O}(dt^3)$ , and since the full time evolution consists in  $(t/dt)$  steps, the expected error on observables at a finite time  $t$  scales like  $\mathcal{O}(dt^2)$  when  $dt \rightarrow 0$ . All errors are controlled, so that our algorithm is numerically exact. To compute the expectation value of a given operator at any time, we can trivially rotate

each fermion appearing in it to the current frame according to Eq. (2), since the frame is given by a quadratic Hamiltonian. Note that step (I) alone would be the traditional interaction picture of the bath, and would lead to entanglement growth. Only the addition of steps (II-III) provides an algorithm that reveals the few-body and low-entanglement character of the underlying state.

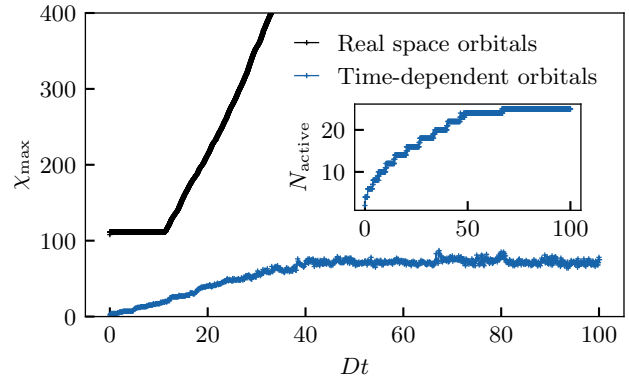


Figure 2. Time-evolution of *few-body revealing*, seen from the maximum bond dimension  $\chi_{\text{max}}$ , for the quench dynamics of IRLM at  $U/D = 0.2$ ,  $V/D = 0.1$ ,  $L = 200$  sites, and Trotter step  $dt = 0.1$ . Our algorithm using time-dependent orbital rotation shows bounded entanglement at long times, while the numerical costs diverge for simulations with real space orbitals. *Inset:* the total number of active orbitals (with  $\chi_a > 1$ ) is also seen to saturate over time, and dynamics remains few-body.

*Results.* We first begin by illustrating the remarkable disentangling feature of our *few-body revealing* algorithm for a quench of the IRLM. Figure 2 shows the time evolution of the maximum bond dimension  $\chi_{\text{max}} = \text{Max}[\chi_a]$ , comparing calculations using the time-dependent orbital basis or the real space basis. While  $\chi_{\text{max}}$  grows unbounded in the latter, it saturates to small values in the former. In addition, the number of active orbitals  $N_{\text{active}}$  in the new algorithm remains bounded at long times, making the scheme controlled and efficient.

A crucial test of the accuracy of our new algorithm is given in Fig. 3. Previous time-dependent NRG and DMRG studies [4] for the same quench protocol have shown that errors could not be decreased below  $10^{-2}$ , preventing a detailed study of charge relaxation at long times. Interestingly, it was predicted [32] that the damping of the charge imbalance at the impurity site,  $n_0(t) - 1/2$ , would crossover from a fully coherent regime (with an infinite number of zeroes) at  $U > U_c$ , to a partially coherent regime (with a finite number of zeroes) for  $0 < U < U_c$ . Such coherent regime, here displaying three zeroes at times  $t_1, t_2, t_3$ , is shown in the main panel of Fig. 3. We extracted these zeroes for many  $U$  values (see inset), and we observe that the first zero  $t_1$  disappears at  $U \rightarrow 0$  as expected from the existence of the

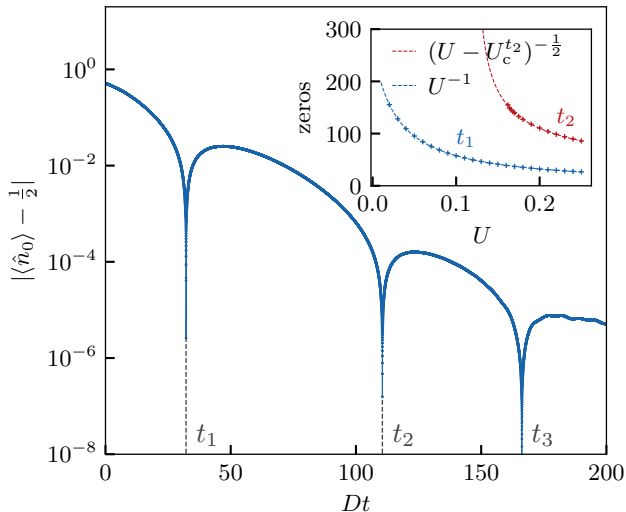


Figure 3. Impurity charge relaxation toward the equilibrium value  $n_0(t \rightarrow \infty) = 1/2$  for the IRLM at  $U/D = 0.2$ ,  $V/D = 0.1$ ,  $L = 200$  sites, and Trotter step  $dt = 0.01$ . The dynamics for  $U > 0$  is coherent, with a leading exponential envelope, and a certain number of zeroes indicated as  $t_1, t_2, t_3$  here. *Inset*: the first zero  $t_1$  diverges as  $1/U$  for  $U \rightarrow 0$  (in agreement with analytical results extracted from Ref. [32]), while the second zero  $t_2$  is found to diverge at finite  $U_c^{t_2}/D \simeq 0.12$  with a different power law  $(U - U_c^{t_2})^{-\frac{1}{2}}$ .

incoherent regime at  $U \leq 0$  [33], and diverges as  $1/U$ , in agreement with the analytics of Ref. [32]. Interestingly, we find that the subsequent zero  $t_2$  diverges at a finite  $U_c^{t_2}$ , a new observation implying that relaxation occurs via a unique zero  $t_1$  for  $0 < U < U_c^{t_2}$ . This is compatible with (yet clearly beyond) the predictions of Ref. [32]. In addition, we are able to identify a different power law behavior  $t_2 \propto (U - U_c^{t_2})^{-\frac{1}{2}}$  governing the disappearance of the second zero. Our study surmounts a numerical challenge, because it requires controlling all errors down to  $10^{-6}$ , as detailed in Sec. III of Ref. [28].

We finally investigate the spatial structures in the environment at long times after the quench for the IRLM at negative  $U/D = -0.2$  (Kondo regime, corresponding to a large relaxation time  $DT \simeq 100$ ), for a very large system with  $L = 2000$  sites. Such dynamics can be easily computed in the non-interacting case [28, 34], but is very challenging in presence of interactions. Focusing on the local charge  $\langle \hat{n}_i \rangle$  (top panel of Fig. 4), we see that the extra density moves away ballistically from the impurity located at site  $i = 0$ , without any damping or dispersion. Spatial Kondo correlations, given by the observable  $|\langle \hat{n}_0 \hat{n}_i \rangle - \langle \hat{n}_0 \rangle \langle \hat{n}_i \rangle|$ , have been the topic of intense studies for the ground state of impurity models [35]. While Numerical Renormalization Group (NRG) simulations are feasible in and out of equilibrium [36, 37], they require the expensive construction of a double bath for each computed distance in the chain, while our simula-

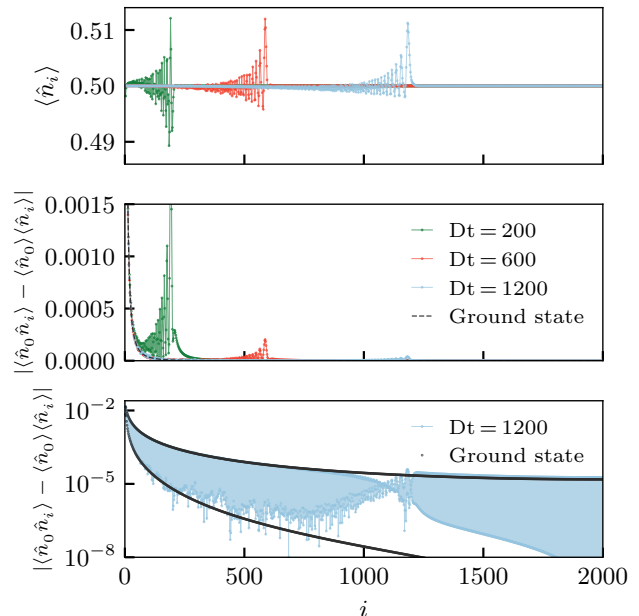


Figure 4. *Top*: Local charge  $\langle \hat{n}_i \rangle$  on site  $i$  for a long chain of  $L = 2000$  sites, with  $U/D = -0.2$ ,  $V/D = 0.1$ , and Trotter step  $dt = 0.1$ , showing the ballistic motion of the charge wavepacket at three different times. *Middle*: charge correlation function  $|\langle \hat{n}_0 \hat{n}_i \rangle - \langle \hat{n}_0 \rangle \langle \hat{n}_i \rangle|$  for the same parameters as the top panel, only on even sites. At distances  $i \ll Dt$ , a charge Kondo cloud binds progressively to the impurity. At distances  $i \simeq Dt$ , a ballistic peak of correlations between the local charge  $\hat{n}_i$  in the wavepacket and the impurity charge  $\hat{n}_0$  is seen, that decays in amplitude as  $t \rightarrow \infty$ , due to loss of entanglement outside the Kondo cloud. *Bottom*: same plot as the middle panel, but for both even/odd sites, now on a logarithmic scale and only for the time  $Dt = 1000$ . The comparison to the ground state solution (lines) shows proper relaxation to the Kondo cloud for  $i \ll Dt$ , and also the formation of a dynamical cloud for  $i \gtrsim Dt$ , despite the fact that the excess charge is vanishing after the wavefront (top panel).

tion is done with only one bath, and the computation of any observable is single shot. Errors are also maintained below  $10^{-4}$  on all sites in our calculation. For the quench, we find several remarkable observations in these spatial correlations. First, at short distances  $0 < i \ll Dt$  compared to the wavepacket, a Kondo cloud bound to the impurity progressively forms, see middle/bottom panels of Fig. 4 (for linear/logarithmic views). This constitutes a non-trivial check that the relaxation to equilibrium is correctly established in our numerics. Second, we observe a peak of correlations on sites that take part in the wavefront, namely for  $i \lesssim Dt$  (middle panel). The emitted charge wavepacket, although it is spread over hundred of sites, maintains a finite entanglement to the impurity. Relaxation to equilibrium is nevertheless reached at  $t \rightarrow \infty$ , since these correlations decay at long times, while the excess charge remains constant in amplitude. Third,

we reveal new details on the Kondo-like correlations that emerge in front of the wavepacket for sites at distances  $i \gtrsim D.t$  (bottom panel). While “supra-luminous” correlations are expected [37], they remarkably reach very long distances beyond the wavefront, in a region of space where charge neutrality is exactly balanced, and quantitatively differ from the Kondo cloud correlations that are bound to the impurity. A full movie of the dynamics is available here [38].

*Outlook.* Using optimal time-dependent orbital rotations, we showed that *few-body revealing* makes the quench dynamics of quantum impurities almost trivial (namely few-body and low entangled). This finding gives rise to a numerically exact algorithm that is very simple to implement, faster and more accurate than previous state of the art, and able to cope with macroscopically large systems and long times. This advance opens obviously many promising perspectives for the dynamical simulations of interacting quantum systems. For spinful Anderson quantum impurities, the spatio-temporal dynamics of spin-charge separation could be explored, possibly at finite temperature with a thermofield approach [39]. Generalizing orbital rotations to superconducting quantum dots [40] should also open the possibility to study the dynamics of interacting Andreev bound states. Interaction effects in electronic waveguides [41], often neglected [42], could also be investigated. Another promising route concerns real-time quantum impurity solvers for the DMFT equations [2], especially in the multi-orbital case, and in the context of out-of-equilibrium physics [43], a fascinating and challenging topic [44]. Finally, extensions of time-dependent orbital rotation to bosons and two-level systems could help the simulation of driven superconducting qubits [45] and quantum processing platforms [46].

*Acknowledgements.* YNF and SF were supported by the PEPR integrated project EPiQ ANR-22-PETQ-0007 part of Plan France 2030. MD was supported by the Deutsche Forschungsgemeinschaft through the cluster of excellence ML4Q (EXC 2004, project-id 390534769) and by the Deutsche Forschungsgemeinschaft through CRC 1639 NuMeriQS (project-id 511713970). We also thank T.Costi, V. Meden, and I. Snyman for stimulating discussions.

---

[1] R. Bulla, T. A. Costi, and T. Pruschke, *Rev. Mod. Phys.* **80**, 395 (2008).  
 [2] A. Georges, G. Kotliar, W. Krauth, and M. J. Rozenberg, *Rev. Mod. Phys.* **68**, 13 (1996).  
 [3] K. Le Hur, P. Doucet-Beaupré, and W. Hofstetter, *Phys. Rev. Lett.* **99**, 126801 (2007).  
 [4] H. T. M. Nghiem, D. M. Kennes, C. Klöckner, V. Meden, and T. A. Costi, *Phys. Rev. B* **93**, 165130 (2016).  
 [5] H. T. M. Nghiem and T. A. Costi, *Phys. Rev. B* **90**,

035129 (2014).  
 [6] Y. Núñez Fernández, M. Jeannin, P. T. Dumitrescu, T. Kloss, J. Kaye, O. Parcollet, and X. Waintal, *Phys. Rev. X* **12**, 041018 (2022).  
 [7] G. Cohen and E. Rabani, *Phys. Rev. B* **84**, 075150 (2011).  
 [8] H. Shinaoka, E. Gull, and P. Werner, *Computer Physics Communications* **215**, 128 (2017).  
 [9] J. Thoenniss, M. Sonner, A. Leroose, and D. A. Abanin, *Phys. Rev. B* **107**, L201115 (2023).  
 [10] B. Kloss, J. Thoenniss, M. Sonner, A. Leroose, M. T. Fishman, E. M. Stoudenmire, O. Parcollet, A. Georges, and D. A. Abanin, *Phys. Rev. B* **108**, 205110 (2023).  
 [11] G. Park, N. Ng, D. R. Reichman, and G. K.-L. Chan, *Phys. Rev. B* **110**, 045104 (2024).  
 [12] F. B. Anders and A. Schiller, *Phys. Rev. Lett.* **95**, 196801 (2005).  
 [13] M. Lotem, A. Weichselbaum, J. von Delft, and M. Goldstein, *Phys. Rev. Res.* **2**, 043052 (2020).  
 [14] P. B. Vigman and A. M. Finkel’shtein, *Sov. Phys. JETP* **48**, 102 (1978).  
 [15] R.-Q. He and Z.-Y. Lu, *Phys. Rev. B* **89**, 085108 (2014).  
 [16] M. Debertolis, S. Florens, and I. Snyman, *Phys. Rev. B* **103**, 235166 (2021).  
 [17] M. Debertolis, I. Snyman, and S. Florens, *Phys. Rev. B* **106**, 125115 (2022).  
 [18] S. Florens and I. Snyman, *Phys. Rev. B* **92**, 195106 (2015).  
 [19] T. Shi, E. Demler, and J. I. Cirac, *Annals of Physics* **390**, 245 (2018).  
 [20] S. Bravyi and D. Gosset, *Commun. Math. Phys.* **356**, 451 (2017).  
 [21] I. Snyman and S. Florens, *Phys. Rev. B* **104**, 195136 (2021).  
 [22] S. Boutin and B. Bauer, *Phys. Rev. Res.* **3**, 033188 (2021).  
 [23] A.-K. Wu, B. Kloss, W. Krinitsin, M. T. Fishman, J. H. Pixley, and E. M. Stoudenmire, *Phys. Rev. B* **111**, 035119 (2025).  
 [24] C. Krumnow, L. Veis, O. Legeza, and J. Eisert, *Phys. Rev. Lett.* **117**, 210402 (2016).  
 [25] C. Krumnow, J. Eisert, and O. Legeza, arXiv:1904.11999.  
 [26] D. J. Thouless, *Nucl. Phys.* **21**, 225 (1960).  
 [27] M. T. Fishman and S. R. White, *Phys. Rev. B* **92**, 075132 (2015).  
 [28] See Supplemental Material.  
 [29] E. Anderson, *Discontinuous plane rotations and the symmetric eigenvalue problem* (University of Tennessee, 2000) in LAPACK Working Note 150.  
 [30] S. R. White and A. E. Feiguin, *Phys. Rev. Lett.* **93**, 076401 (2004).  
 [31] M. Fishman, S. R. White, and E. M. Stoudenmire, *SciPost Phys. Codebases*, 4 (2022).  
 [32] D. M. Kennes, O. Kashuba, M. Pletyukhov, H. Schoeller, and V. Meden, *Phys. Rev. Lett.* **110**, 100405 (2013).  
 [33] A. J. Leggett, S. Chakravarty, A. T. Dorsey, M. P. A. Fisher, A. Garg, and W. Zwerger, *Rev. Mod. Phys.* **59**, 1 (1987).  
 [34] V. Eisler and I. Peschel, *Journal of Statistical Mechanics: Theory and Experiment* **06**, P06005 (2007).  
 [35] I. Affleck, *Kondo Screening Cloud: What it is and how to observe it* (World Scientific, Singapore, 2010) in *Perspectives of Mesoscopic Physics*.  
 [36] L. Borda, *Phys. Rev. B* **75**, 041307(R) (2007).

- [37] B. Lechtenberg and F. B. Anders, Phys. Rev. B **90**, 045117 (2014).
- [38] <http://perso.neel.cnrs.fr/serge.florens/docs/evolution.gif>
- [39] L. Kohn and G. E. Santoro, Journal of Statistical Mechanics: Theory and Experiment **2022**, 063102 (2022).
- [40] V. V. Baran, E. J. P. Frost, and J. Paaske, Phys. Rev. B **108**, L220506 (2023).
- [41] G. Roussely, E. Arrighi, G. Georgiou, S. Takada, M. Schalk, M. Urdampilleta, A. Ludwig, A. D. Wieck, P. Armagnat, T. Kloss, X. Waintal, T. Meunier, and C. Bäuerle, Nature Communications **9**, 2811 (2018).
- [42] T. Kloss and X. Waintal, arXiv:2502.03428.
- [43] H. Aoki, N. Tsuji, M. Eckstein, M. Kollar, T. Oka, and P. Werner, Rev. Mod. Phys. **86**, 779 (2014).
- [44] A. Picano, G. Biroli, and M. Schirò, arXiv:2405.19884.
- [45] R. Shillito, A. Petrescu, J. Cohen, J. Beall, M. Hauru, M. Ganahl, A. G. Lewis, G. Vidal, and A. Blais, Phys. Rev. Appl. **18**, 034031 (2022).
- [46] M. Ganahl, J. Beall, M. Hauru, A. G. Lewis, T. Wójcicki, J. H. Yoo, Y. Zou, and G. Vidal, PRX Quantum **4**, 010317 (2023).

## Supplemental material for “Resolving space-time structures of quantum impurities with time-dependent orbitals”

### I. EXTRACTING SINGLE ORBITAL USING QUANTUM GATES

In the following we explain how we build a convenient set of quantum gates that moves a given orbital  $\mathbf{v} = (v_1, v_2, \dots, v_L)$  to the first site. We mainly follow Ref. [27] of the main text. An elementary or Givens rotation is defined as the  $2 \times 2$  unitary matrix

$$G_\theta = \begin{pmatrix} c & s \\ -\bar{s} & c \end{pmatrix}, \quad (\text{S1})$$

with  $c = \cos \theta$ ,  $s = \sin \theta$  and  $\theta$  a complex number. Particularly,

$$G_\theta \cdot \begin{pmatrix} p \\ q \end{pmatrix} = \begin{pmatrix} r \\ 0 \end{pmatrix} \text{ if } \tan \bar{\theta} = q/p, \quad (\text{S2})$$

and we say that the second component of the vector is eliminated by  $G_\theta$ , see Ref. [29] of the main text. The key point is to transform the orbital (or normalized eigenvector) to an elementary vector  $\mathbf{e}_1 = (1, 0, 0, \dots, 0)$  using elementary rotations, that is,

$$G_{\theta_1}^1 G_{\theta_2}^2 \dots G_{\theta_{L-1}}^{L-1} \mathbf{v} \equiv G \cdot \mathbf{v} = \mathbf{e}_1, \quad (\text{S3})$$

where  $G_{\theta_i}^i$  acts on the rows  $i$  and  $i+1$  eliminating the component  $i+1$ . Since  $G$  is a unitary matrix we can check that the eigenvalue equation  $A\mathbf{v} = \lambda\mathbf{v}$  implies  $(GAG^\dagger)_{11} = \lambda$  where  $GAG^\dagger$  and  $A$  are similar matrices. In words, we can extract the orbital  $\mathbf{v}$  by moving to the frame  $G$ . Among all possible frames doing this,  $G$  is very special because it consists of only one layer of nearest neighbor elementary rotations. Each elementary

rotation is mapped to a quantum gate by introducing a Fock basis  $\{|00\rangle, |10\rangle, |01\rangle, |11\rangle\}$  for the two sites involved in the rotation of the state  $|\psi(t)\rangle$ , leading to the following map:

$$G_\theta \longrightarrow \hat{G}_\theta \equiv \begin{pmatrix} 1 & 0 & 0 & 0 \\ 0 & c & -\bar{s} & 0 \\ 0 & s & c & 0 \\ 0 & 0 & 0 & 1 \end{pmatrix}. \quad (\text{S4})$$

### II. EXACT DYNAMICS IN THE NON-INTERACTING CASE

In order to test carefully our general MPS algorithm, we derive an exact formal solution for the resonant level model, corresponding to the non-interacting case of the problem studied in the main text. We start with the free real-space Hamiltonian:

$$\begin{aligned} \hat{H}_0 &= V(c_0^\dagger c_1 + c_1^\dagger c_0) + \frac{D}{2} \sum_{j=1}^{L-1} (\hat{c}_j^\dagger \hat{c}_{j+1} + \text{h.c.}) \\ &= V(\hat{c}_0^\dagger \hat{c}_1 + \hat{c}_1^\dagger \hat{c}_0) + \sum_{k=2}^{L-1} \epsilon_k \tilde{c}_k^\dagger \tilde{c}_k + V' \sum_{k=2}^{L-1} (\hat{c}_1^\dagger \tilde{c}_k + \text{h.c.}) \end{aligned} \quad (\text{S5})$$

expressing the fermionic chain operators in Fourier space as  $\hat{c}_j = (L-2)^{-1/2} \sum_{k=2}^{L-1} \tilde{c}_k e^{i2\pi(j-2)(k-2)/(L-2)}$  for sites  $j = 2, \dots, L-1$ . The coupling to the bath now reads  $V' = (L-2)^{-1/2} D/2$  and the one-particle energy of the chain is given by  $\epsilon_k = -D \cos[2\pi(k-2)/(L-2)]$  for  $k = 2, \dots, L-1$ .

The initial state  $|\psi(0)\rangle$  at time  $t = 0$  considered in the main text corresponds to having site  $j = 0$  occupied, site  $j = 1$  empty, and the rest of the chain decoupled from the impurity, which therefore reads as a product state involving the  $\tilde{c}_k$  orbitals with negative energy (at half-filling):

$$|\psi(0)\rangle = \hat{c}_0^\dagger \prod_{\epsilon_k < 0} \tilde{c}_k^\dagger |0\rangle. \quad (\text{S6})$$

We relabel all the fermionic fields as  $\hat{f}_a$ , with  $\hat{f}_0 = \hat{c}_0$ ,  $\hat{f}_1 = \hat{c}_1$ ,  $\hat{f}_a = \tilde{c}_a$  (for  $a = 2, \dots, L-1$ ) for compactness.

We now define the one-body (correlation) matrix at a given time  $t$  as  $\rho_{ab}(t) = \langle \psi(t) | \hat{f}_a^\dagger \hat{f}_b | \psi(t) \rangle$ , which reads in Heisenberg picture  $\rho_{ab}(t) = \langle \psi(0) | \hat{f}_a^\dagger(t) \hat{f}_b(t) | \psi(0) \rangle$ , with  $\hat{f}_a(t) = e^{i\hat{H}_0 t} \hat{f}_a e^{-i\hat{H}_0 t}$ , where  $\hbar = 1$  has been set. We now express the free Hamiltonian (S5) in its eigenbasis,  $\hat{H}_0 = \sum_{p=0}^{L-1} \Omega_p \hat{\gamma}_p^\dagger \hat{\gamma}_p$ , with the unitary transformation to operators  $\hat{\gamma}_p = \sum_{a=0}^{L-1} U_{pa} \hat{f}_a$ , that can be obtained numerically for a cost  $O(L^3)$  by diagonalizing the one-particle Hamiltonian  $h_{ab}$  with matrix elements  $h_{aa} = \epsilon_a \theta(a-1)$ ,  $h_{a<b} = V \delta_{a0} \delta_{b1} + (D/2) \delta_{a1} \theta(b-1)$ , and  $h_{a>b} = h_{a<b}$ . The time-evolution is now explicitly

expressed as:

$$\begin{aligned}\hat{f}_a(t) &= \sum_{p=0}^{L-1} U_{pa}^* e^{i\hat{H}_0 t} \hat{\gamma}_p e^{-i\hat{H}_0 t} = \sum_{p=0}^{L-1} U_{pa}^* e^{-i\Omega_p t} \hat{\gamma}_p \quad (\text{S7}) \\ &= \sum_{a'=0}^{L-1} \sum_{p=0}^{L-1} U_{pa}^* e^{-i\Omega_p t} U_{pa'} \hat{f}_{a'} \equiv \sum_{a'=0}^{L-1} M_{aa'}(t) \hat{f}_{a'}.\end{aligned}$$

We thus obtain the correlation matrix at time  $t$  as:

$$\rho_{ab}(t) = \sum_{a',b'=0}^{L-1} M_{aa'}^*(t) M_{bb'}(t) \langle \psi(0) | \hat{f}_{a'}^\dagger \hat{f}_{b'} | \psi(0) \rangle. \quad (\text{S8})$$

For the initial state  $|\psi(0)\rangle = \hat{f}_0^\dagger \prod_{\epsilon_a < 0} \hat{f}_a^\dagger |0\rangle$ , the average  $\langle \psi(0) | \hat{f}_{a'}^\dagger \hat{f}_{b'} | \psi(0) \rangle = n_{a'} \delta_{a'b'}$ , with  $n_{a'} = 0$  or 1 the initial occupation of orbital  $a'$ . We finally obtain the real space correlation matrix  $\langle c_i^\dagger c_j \rangle$  by back Fourier transform of Eq. (S8).

### III. BENCHMARKING ERRORS

We now compare results obtained from our numerical algorithm to this exact solution. In Figure S1, we show the impurity hybridization  $\langle \hat{c}_0^\dagger \hat{c}_1 + \hat{c}_1^\dagger \hat{c}_0 \rangle = \rho_{01} + \rho_{10}$  (left panel) and charge  $\langle \hat{c}_0^\dagger \hat{c}_0 \rangle = \rho_{00}$  (right panel) as a function of time  $t$  for two different Trotter discretizations  $dt = 0.1$  and  $dt = 0.01$ . The exact result from Eq. (S8) is subtracted to reveal the convergence of the numerics. Even for the relatively large time step  $dt = 0.1$ , errors are already as small as  $10^{-4}$ . Errors go down to  $10^{-6}$  for  $dt = 0.01$ , confirming the general scaling  $(dt)^2$  of the Trotter discretization.

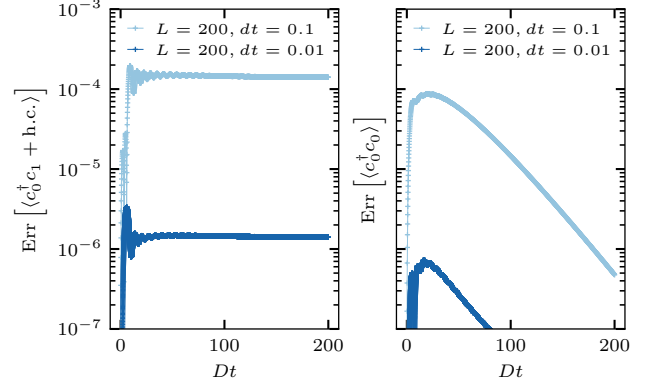


Figure S1. Numerical errors for the impurity hybridization (left panel) and the local charge (right panel) as a function of time, for the quench of the non-interacting resonant level model for  $V/D = 0.1$  and  $L = 200$  sites. The values from the exact solution (S8) were subtracted to the MPS results. The drop from  $10^{-4}$  down to  $10^{-6}$  by diminishing the time step from  $dt = 0.1$  to  $dt = 0.01$  confirms the expected  $(dt)^2$  scaling of the Trotter error.

We can also establish the convergence of the spatial structures. In the top panel of Fig. S2, we plot the error on the local charge  $\langle \hat{n}_i \rangle$  along the chain for a very long system with  $L = 1000$  sites, computed in the non-interacting case  $U = 0$  for  $V/D = 0.1$ , at fixed time  $Dt = 200$  with a Trotter time step  $dt = 0.1$ . Again we have subtracted the exact solution Eq. (S8) to the numerical MPS simulations. The bottom panel shows the error on the Kondo cloud charge correlator  $|\langle \hat{n}_0 \hat{n}_i \rangle - \langle \hat{n}_0 \rangle \langle \hat{n}_i \rangle|$ . For the exact free solution, we can use Wick's theorem, and we find  $|\langle \hat{n}_0 \hat{n}_i \rangle - \langle \hat{n}_0 \rangle \langle \hat{n}_i \rangle| = |\langle \hat{c}_0^\dagger \hat{c}_i \rangle|^2 = |\rho_{0i}|^2$ . For the MPS simulation, the cloud is computed without use of Wick's theorem, as discussed in the main text. Both plots in Fig. S2 show errors at the maximum level of  $10^{-4}$ , demonstrating the complete control of the algorithm over the full many-body wavefunction (and not just on impurity observables).

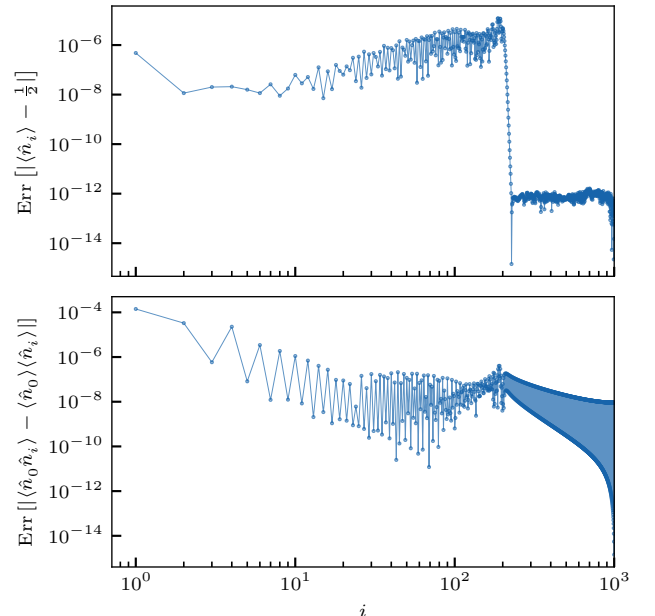


Figure S2. Errors on the local charge (top panel) and on the Kondo cloud charge correlator (bottom panel) as a function of site index  $i$ .